buildings

MDPI

Article

Experimental Investigation on the Seismic Behavior of Precast Concrete Beam-Column Joints with Five-Spiral Stirrups

Jinhu Zheng [1], Zezhou Pan [1], Hao Zhen [1], Xuhua Deng [2], Chumao Zheng [2], Zhenye Qiu [2], Longpan Xie [1], Zhe Xiong [1,*], Lijuan Li [1,*] and Feng Liu [1]

[1] School of Civil and Transportation Engineering, Guangdong University of Technology, Guangzhou 510006, China; 2112109162@mail2.gdut.edu.cn (J.Z.); 3121003163@mail2.gdut.edu.cn (Z.P.); 3122002693@mail.gdut.edu.cn (H.Z.); loongpan@outlook.com (L.X.); fliu@gdut.edu.cn (F.L.)
[2] Guangdong Foundation New Century Concrete Co., Ltd., Guangzhou 510660, China; dengxuhua@gdjc.net (X.D.); zhengchumao@gdjc.net (C.Z.); qiuzhenye@gdjc.net (Z.Q.)
* Correspondence: gdgyxz263@gdut.edu.cn (Z.X.); lilj@gdut.edu.cn (L.L.)

Abstract: Precast concrete structure is a low-carbon building system that has been attracting extensive attention in recent decades. Beam–column joints are the weak links in precast concrete structures. Past studies showed that the five-spiral stirrups had excellent confinement effects and had the potential to enhance the seismic performance of concrete structures. This study proposed the reinforcement of precast concrete beam–column joints by using five-spiral stirrups and investigated their seismic performance. Considering the influences of the joint failure mode, joint type, construction method, and stirrup type, low-cycle loading tests were conducted on six full-scale precast concrete beam–column joint specimens. Various seismic behavior indicators, such as failure modes, hysteresis curves, skeleton curves, ductility, and energy dissipation, were obtained. The results indicated that the deformation capacity of the precast joints with five-spiral stirrups was comparable to that of cast-in-place joints. Under different failure design criteria, the seismic performance of the precast joints was superior to that of cast-in-place joints. Furthermore, the experimental capacities of the precast joints, using five-spiral stirrups, were higher than the calculated values according to the design code, demonstrating an adequate safety margin. This research contributes to the development of low-carbon and sustainable construction practices in the field of precast concrete structures.

Keywords: five-spiral stirrup; precast concrete structure; beam-column joint; seismic behavior; low carbon emission

check for updates

Citation: Zheng, J.; Pan, Z.; Zhen, H.; Deng, X.; Zheng, C.; Qiu, Z.; Xie, L.; Xiong, Z.; Li, L.; Liu, F. Experimental Investigation on the Seismic Behavior of Precast Concrete Beam-Column Joints with Five-Spiral Stirrups. *Buildings* **2023**, *13*, 2357. https://doi.org/10.3390/buildings13092357

Academic Editor: Flavio Stochino

Received: 25 August 2023
Revised: 13 September 2023
Accepted: 14 September 2023
Published: 16 September 2023

Copyright: © 2023 by the authors. Licensee MDPI, Basel, Switzerland. This article is an open access article distributed under the terms and conditions of the Creative Commons Attribution (CC BY) license (https://creativecommons.org/licenses/by/4.0/).

1. Introduction

In many countries, the construction industry is commonly regarded as an import sector of the national economy, but it is also the main source of carbon emissions. The carbon footprint in the construction industry accounts for about 27% of total emissions, causing a significant impact on the environment [1–3]. Prefabrication for structures is usually regarded as an important approach to achieve the "carbon peak" and "carbon neutrality" [4,5]. Statistically, the carbon emissions in prefabricated buildings' life cycles could be reduced by 40% comparing to that of ordinary buildings [6–8]. Owing to the mass production in the prefabricated construction, materials, wastes, and energy consumed in construction would be greatly reduced. In addition, the highly automatic installation methods for prefabricated buildings reduce the noise, waste, and wastewater emissions. Owing to its extensive environmental benefits, prefabricated construction has been a hot research topic in civil engineering. Precast reinforced concrete (RC) frame is the most widely adopted structural form for prefabricated buildings, and it consists of the precast columns, beams, and slabs. The structural behavior of a precast RC frame is mainly governed by the connections between precast members. Past studies on the seismic performance indicated that the damage of precast RC frames mostly occurred in the connections, which are the

weak point of the structural system [9–12]. Therefore, the investigation on improving the seismic performance of the connections is an import aspect to promote the application of the prefabricated construction and to achieve low-carbon development in the construction industry.

Currently, some scholars are trying to improve the seismic performance of precast RC beam–column joints by using high-performance materials and proposing novel joint configurations. Deng et al. [13] applied highly ductile fiber-reinforced concrete into precast concrete beam–column connections, and they conducted a cyclic loading test on the connections. Experimental results indicated that the highly ductile fiber-reinforced concrete could obviously enhance the shear capacity and damage-resistance capacity of the connections, and it could change the failure mode from shear failure to beam-end failure. Guan et al. [14] proposed an innovative, partially precast, steel-reinforced concrete (PPSRC) beam–column connection and experimentally investigated its seismic behavior, finding that the precast connection had higher strength, better ductility, and higher energy dissipation capacity than the on-situ cast connection. Huang et al. [15] proposed a new type of replaceable dry connection for the precast beam–column joint, and its load-bearing capacity, stiffness, energy dissipation capacity, and deformation capacity are superior to the cast-in-place joint. Obviously, implementing high-performance materials and improving connection configurations could enhance the seismic performance of precast RC beam–column joints [16,17]. Nevertheless, high-performance materials have high prices, and their widespread use in structures will result in higher engineering costs. In addition, quality control of construction is vital for the seismic behavior of RC beam–column joints in real projects. The adoption of new joint configurations for precast joints may complicate the construction process and increase the difficulty in concrete casting [18], resulting in the concern that the joints, in practice, cannot reach the expected seismic performance obtained in laboratories. Therefore, it is necessary to investigate new types of precast RC beam–column joints that have higher feasibility in engineering practice.

The five-spiral stirrup has the potential to enhance the seismic performance of the precast beam–column joint owing to its features of desirable continuity, high confining effect, and convenience in fabrication [19,20]. The five-spiral stirrup consists of four small stirrups, in column corners, to offer high confinement on the concrete in corners and a large stirrup to laterally reinforce the whole section and fix the longitudinal rebars [21]. Several studies were conducted on the seismic behavior of RC columns reinforced by five-spiral stirrups, and the confining effect on enhancing the seismic behavior was investigated. Yin et al. [22] conducted a cyclic loading test (axial compression and lateral cyclic loading) on RC columns, with 10 different types of stirrups, and found that the RC columns with spiral stirrups have higher strength and ductility than the conventional RC columns, among which the five-spiral configuration exhibited the best performance. Fang et al. [23] investigated the axial compression behavior of seawater sea–sand concrete columns reinforced with fiber reinforced polymer (FRP) five-spiral stirrups, and this stirrup type could enhance the deformability of columns. Xiong et al. [19] experimentally investigated the seismic behavior of seawater sea–sand concrete columns with various types of FRP stirrups and found that the five-spiral configuration of stirrups could significantly enhance the seismic performance of columns compared to the rectangular stirrups.

In the column test, the five-spiral stirrups showed obvious confining effects and greatly enhanced the load-bearing capacity of columns [24]. In Taiwan, China, rectangular concrete columns with five-spiral stirrups have been well-used in precast concrete structures and have undergone seismic tests [25]. However, there is still a lack of studies on the seismic behavior of precast RC beam–column joints reinforced with five-spiral stirrups. The successful application of this novel stirrup into precast beam–column joints will certainly improve the seismic performance of the joints and promote the "low carbon" development of the construction industry. To investigate the seismic behavior of precast RC beam–column joints reinforced with five-spiral stirrups, six full-scale RC joints were tested under cyclic loads. The tested specimens were classified into two groups based on the expected failure

modes, namely "beam-end failure" and "joint failure", and each group contained three specimens, including an interior precast joint, an exterior precast joint, and an exterior cast-in-place joint. This study mainly investigated the failure modes, hysteresis behavior, skeleton curves, strength degradation, stiffness degradation, ductility, and energy dissipation of the precast and cast-in-place joints, under cyclic loads, to understand their seismic behavior. In addition, load-bearing capacities of the joint with five-spiral stirrups were predicted for design purposes. Generally, this study will contribute to the improvement of the design methods of precast RC structures and promote their applications.

2. Experimental Program

2.1. Specimens

There were six full-scale RC joints tested in this study, whose column height was 1.625 m with cross-section size of 450 mm × 450 mm, and beam length was 1.475 m with cross-section size of 250 mm × 450 mm (Figure 1). The specimen variables included the intended failure modes (beam-end failure "S" and joint failure "W"), joint types (interior "I" and exterior "E" joints), construction methods (precast and cast-in-place joint), and stirrup types (five-spiral "F" stirrups for precast joints and rectangular compound stirrups "C" for cast-in-place joints) in the joint core area. The expected failure mode was achieved by setting the reinforcement ratios. Based on the seismic design requirement, joints failed at beam ends were preferred, and it could be achieved by adopting the principle of "strong joint & weak members, strong column & weak beam" in design. Failures of these joints were controlled by the bending capacity of the beams. Nevertheless, past surveys on the seismic damage of structures indicated that the failure in the joint core zone (denoted as joint failure for simplicity) still extensively existed [9–12]. Therefore, both beam-end failure and joint failure specimens were included in this study. In typical frame beam–column joints, the number of interior joints and exterior joints is the majority, which play a major seismic energy dissipation role under earthquake action. Therefore, in this experiment, the interior joints and exterior joints of the frame are selected as the test joint specimens. Details of the specimens are shown in Table 1.

Table 1. Experimental scheme.

No.	Design Criteria	Joint Types	Construction Methods	Joint Stirrup Types	Column Stirrup Types	Beam Stirrup Types
SI-F	Beam-end failure (strong joint—weak beam)	Interior beam-column joint	Precast	Five-spiral stirrup	Five-spiral stirrup	Rectangular stirrup
SE-F		Exterior beam-column joint	Precast	Five-spiral stirrup	Five-spiral stirrup	
SE-C		Exterior beam-column joint	Cast-in-place	Rectangular compound stirrup	Rectangular compound stirrup	
WI-F	Joint failure (weak joint—strong beam)	Interior beam-column joint	Precast	Five-spiral stirrup	Five-spiral stirrup	
WE-F		Exterior beam-column joint	Precast	Five-spiral stirrup	Five-spiral stirrup	
WE-C		Exterior beam-column joint	Cast-in-place	Rectangular compound stirrup	Rectangular compound stirrup	

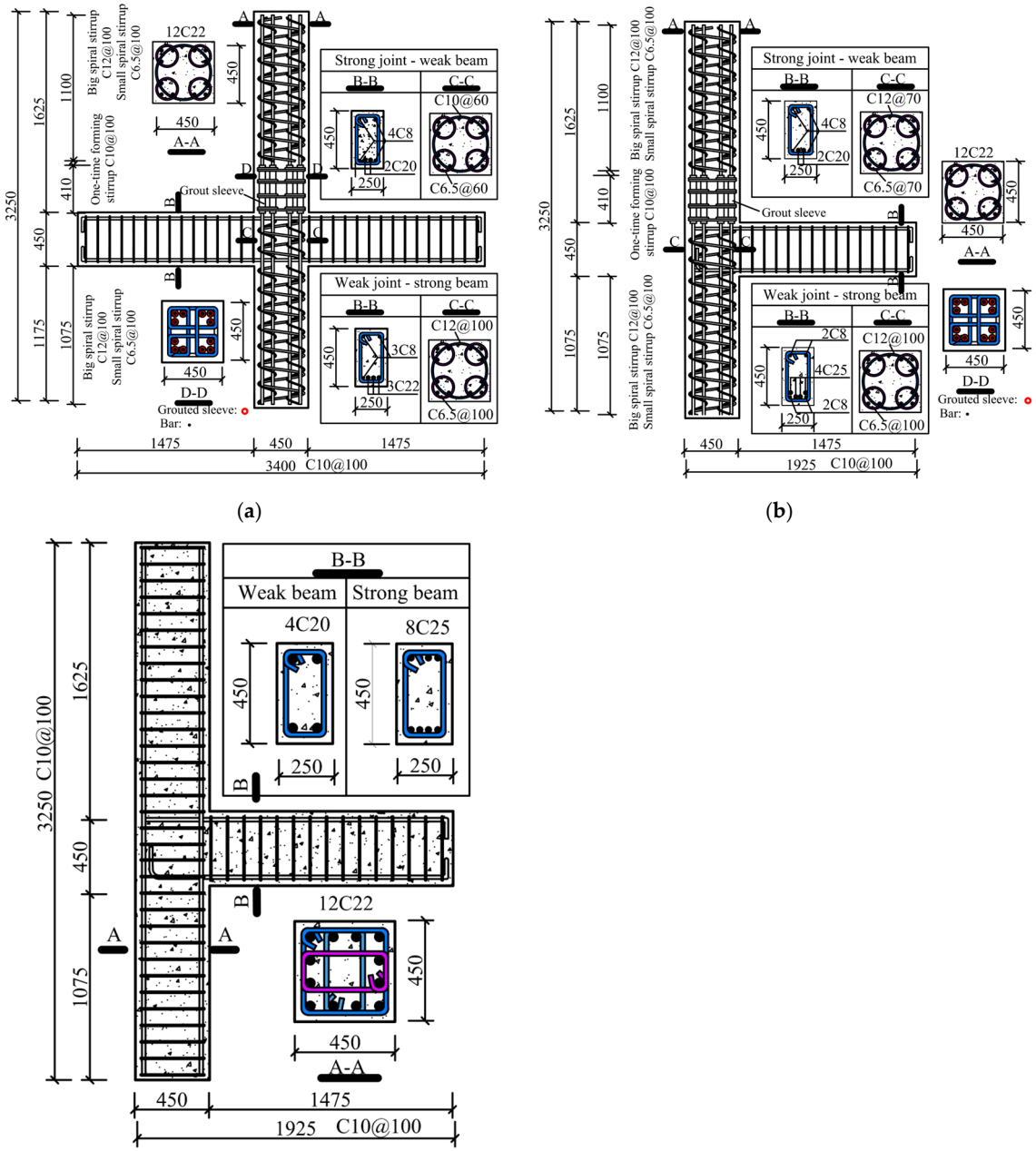

Figure 1. Beam–column joint specimens: (**a**) SI-F and WI-F; (**b**) SE-F and WE-F; (**c**) SE-C and WE-C.

Specimen dimensions and reinforcement details are shown in Figure 1. The longitudinal steel reinforcing bars of the beams and columns were in HRB400 grade. There were 12 longitudinal rebars with diameters of 22 mm in columns of precast joints. For precast specimens expected to fail at beam ends, four 20 mm diameter longitudinal rebars (i.e., two rebars in top and the other two in bottom) were set in the beams, whereas there were six 22 mm diameter longitudinal rebars (i.e., three in top and the other three in bottom) in the beams of joints that would be failed in the core zone. For cast-in-place joints, there were twelve 22 mm diameter rebars in the columns. There were four 20 mm diameter rebars and eight 25 mm diameter rebars set in the beams of cast-in-place joints with target failure modes of beam-end failure and joint failure, respectively. The five-spiral stirrups were used for precast joints, and the details are shown in Figure 2, consisting of a large stirrup (HRB400, 12 mm diameter) and four small stirrups (HPB335, 6 mm diameter). Spacing of the stirrups was 60 mm for the core zone and 100 mm for other regions of columns. Rectan-

gular compound stirrups with diameters of 10 mm were used for the cast-in-place columns, and the spacings were 60 mm and 100 mm for the core-zone and other zones, respectively. Rectangular two-leg stirrups were used for beams in both precast and cast-in-place joints, whose diameters were 10 mm and spacings were 100 mm.

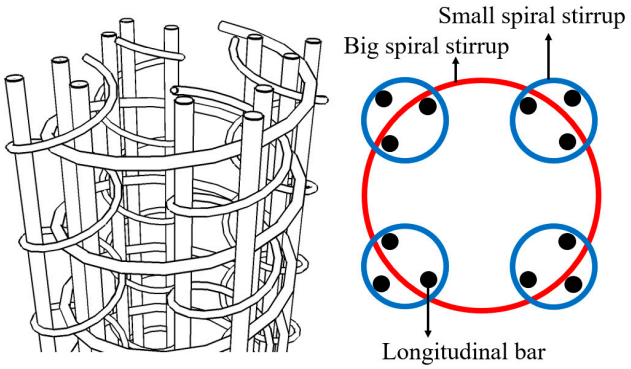

Figure 2. Five-spiral stirrup.

The connection between precast columns and beams was achieved by cast-in-place concrete (i.e., wet joint). Fabrication procedures of the precast specimens are illustrated in Figure 3, which includes (1) placement of steel reinforcing bars; (2) concrete casting and curing for 7 days for precast columns with embedded sleeves and beams with 150 mm thick cast-in-place concrete layer; (3) the installation of precast columns and beams and the on-site casting of concrete for the joint core zone and beam topping; (4) connection of the longitudinal rebars of the upper and lower columns by grouted sleeves. A cyclic loading test was then conducted after the grout reached the design strength (35 N/mm^2). The cast-in-place specimens were prepared according to the construction procedures of conventional in-situ concrete structures.

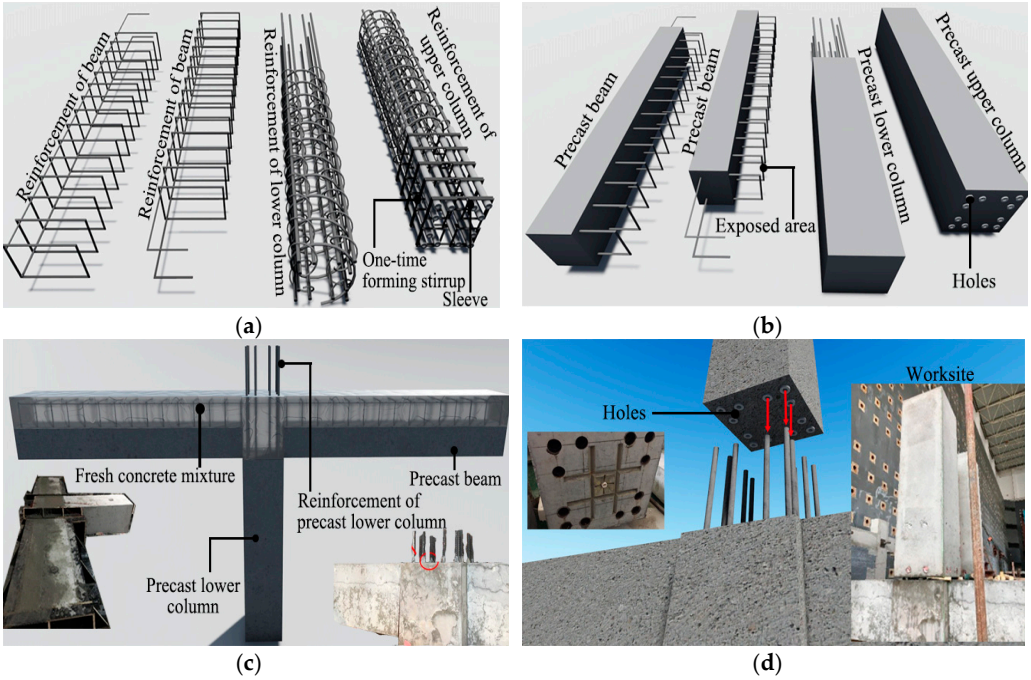

Figure 3. Fabrication process of the precast joints: (**a**) reinforcement perspective; (**b**) precast beams and precast columns; (**c**) assembling process; (**d**) connecting the precast upper column.

2.2. Material Properties

The grade of the concrete was C30, and the mixing ratio was 0.38–1.00–1.11–2.72 for water–cement–fine aggregate–coarse aggregate. There were six 150 mm × 150 mm × 150 mm concrete cubes prepared for each joint to measure the concrete strength. These concrete cubes were cured at a temperature of 20 ± 2 °C and a relative humidity of >95%. The 7 day and 28 day cubic compressive strengths ($f_{cu,k}$) were measured according to [26], and the results are listed in Table 2. The cyclic test was conducted right after the concrete material test. The steel grade of longitudinal rebars was HRB400, and their diameters included 20 mm, 22 mm, and 25 mm, which were denoted as C20, C22, and C25 for the material test. Diameters of stirrups were 12 mm, 10 mm, and 6.5 mm, and they were labeled as C12, C10, and C6.5, respectively. HPB335 steel was used for the small spiral stirrups, whereas HRB400 steel was used for all the other stirrups. Mechanical properties of steel reinforcements were measured according to [27], and the results are listed in Table 3, where f_{sy} is the yield strength, f_{su} is the ultimate strength, E_s is the Young's modulus and ε_{sy} is the yielding strain.

Table 2. Compressive strength of concrete.

No.	SI-F	SE-F	SE-C	WI-F	WE-F	WE-C
7 day $f_{cu,k}$ (MPa)	25.0	26.8	26.7	25.0	25.0	25.8
28 day $f_{cu,k}$ (MPa)	33.0	35.0	35.9	33.2	34.1	34.9

Table 3. Mechanical properties of reinforcing bars.

No.	f_{sy} (MPa)	f_{su} (MPa)	E_s (MPa)	ε_{sy} (10^{-6})
C6.5	382.7	551.9	2.04×10^5	1913.5
C10	436.1	574.6	2.08×10^5	2096.5
C12	454.7	602.4	2.07×10^5	2196.6
C20	442.3	576.2	2.00×10^5	2211.5
C22	429.1	576.0	2.01×10^5	2134.8
C25	441.0	591.0	2.02×10^5	2183.2

2.3. Grouted Sleeve Connection

Connection of the longitudinal rebars of the columns was achieved by using the grouted sleeve joint, as shown in Figure 4. Outer diameter and length of the sleeve were 55 mm and 410 mm, respectively. The diameter of the connected longitudinal rebars was 22 mm, and their yield strength and ultimate strength were 438.5 MPa and 585.5 MPa, respectively. The inserted lengths of the rebars in the sleeve were 190 mm and 200 mm. Compressive strength of the grouted material was 93.88 MPa. Before casting the in-situ concrete of the precast joints, properties of the sleeves were measured using the monotonic and cyclic tests, and the key results are summarized in Table 4, where f_y is the yield strength, f_t the ultimate tensile strength, A_{sgt} is the elongation rate, u_0 is the residual deformation by the monotonic test, and u_{20}, u_4 and u_8 are the residual deformation after 20, 4, and 8 cycles, respectively. The experimental results demonstrated that the grouted sleeve connection had desirable performance and could ensure the integrity of the connection for precast joints.

Table 4. Mechanical properties of grouted sleeve.

f_y (MPa)	f_t (MPa)	A_{sgt} (%)	u_0 (mm)	u_{20} (mm)	u_4 (mm)	u_8 (mm)
452.12	598.75	11.15	0.045	0.015	0.13	0.33

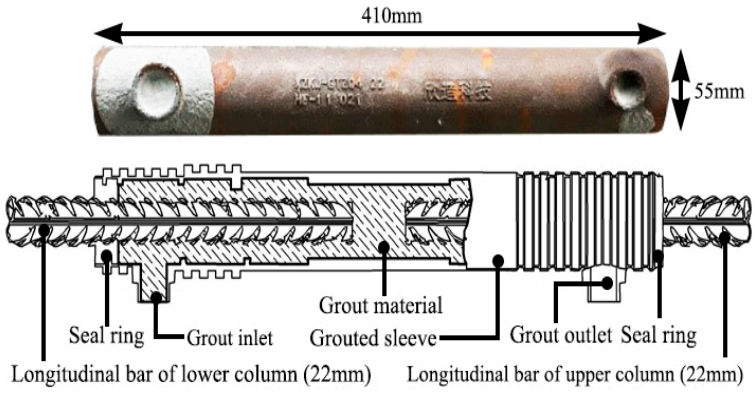

Figure 4. Profile of grouted sleeve.

2.4. Experimental Setup and Instrumentation

In this study, the axial and lateral loads were applied at the column top, as shown in Figure 5. Sliding and hinged supports were set for the column top and column bottom, respectively. Movable hinged support was adopted for the beam ends. The cyclic lateral load was applied using a 300 ton electro-hydraulic servo actuator with displacement control. The axial compressive load was applied using a 500 ton electric hydraulic jack at column top, and the axial force ratio (i.e., the ratio of applied load-to-compressive capacity) was set as 0.1. The axial force was measured by the load cell set between the column top and jack. The load displacement curve of the specimen was directly measured by a 300 ton electro-hydraulic servo actuator. More details of the test setup are given in Figure 5 for both interior and exterior joints. The layout of linear variable displacement transducers (LVDT) is shown in Figure 6 to measure the deformation of the joint core region. The loading regime of the lateral cyclic load is shown in Figure 7. The displacements for the first 4 steps (i.e., I, II, III and IV) were 2.5 mm, 5 mm, 7.5 mm, and 10 mm, respectively. Thereafter, the displacement increment was set as 10 mm. Additionally, one-cycle was adopted for the first three displacements (i.e., I, II and III), and there were three cycles for the other displacement steps [28]. The experiment was terminated when the applied load dropped to 80% of the peak load or obvious failure in the specimen occurred.

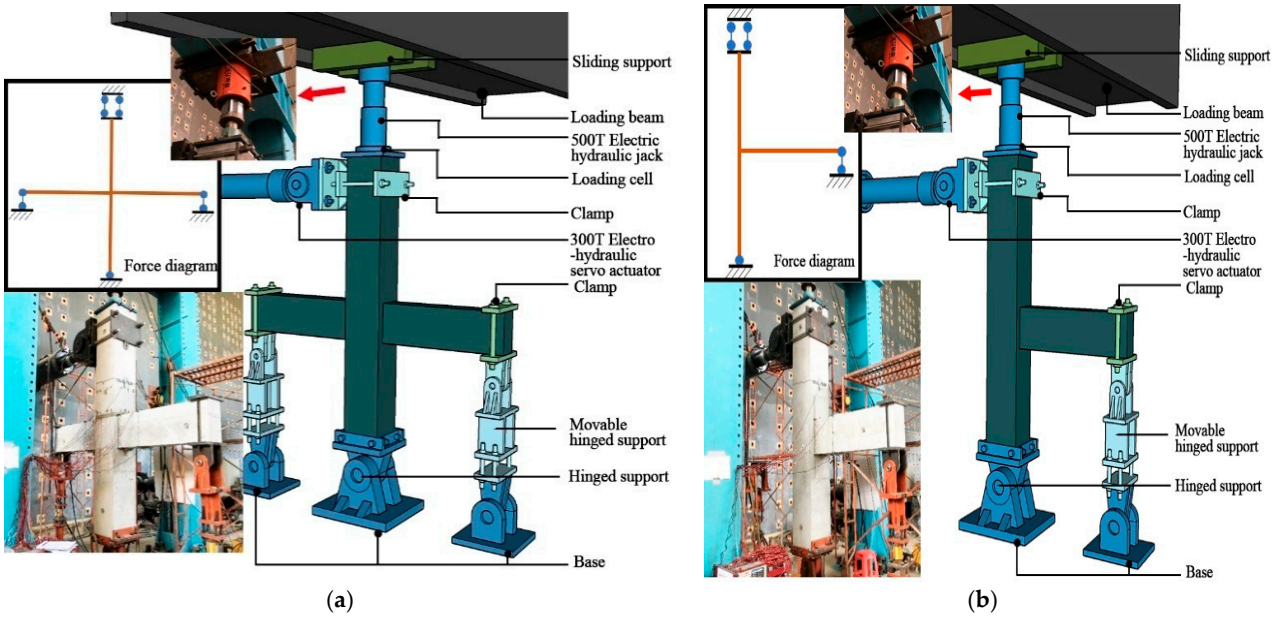

Figure 5. Test setup: (**a**) interior beam-column joints; (**b**) precast beams and precast columns.

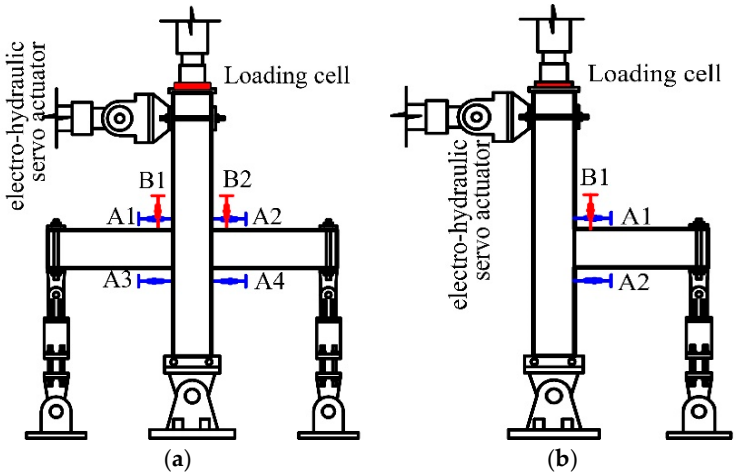

Figure 6. Layout of LVDTs: (**a**) interior beam-column joints; (**b**) exterior beam-column joints.

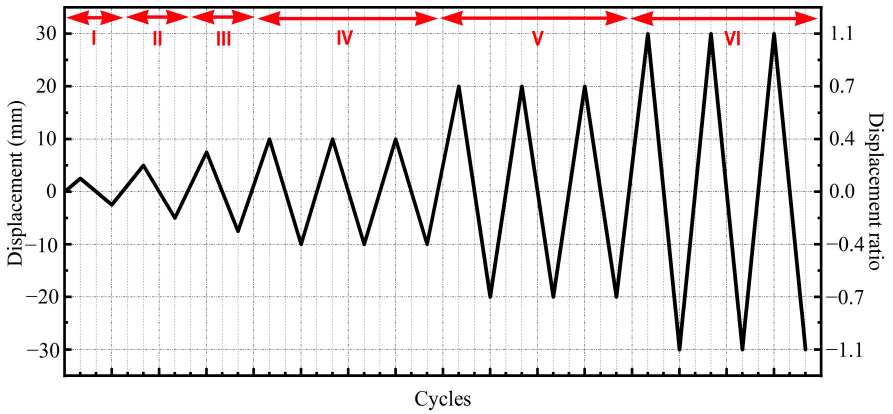

Figure 7. Loading scheme for lateral load.

3. Experimental Results and Discussions

3.1. Failure Modes

Cracking patterns and failure modes of the tested specimens are shown in Figure 8. For specimens designed by the principle of strong joint and weak beam (i.e., SI-F, SE-F, and SE-C), bending failures of beams were observed. The first crack at the beam bottom near the joint zone was observed for the exterior joints (i.e., SE-F and SE-C) when the lateral displacement reached 5 mm, whereas the crack started to appear at 7.5 mm lateral displacement for the interior joint (i.e., SI-F). This is due to the fact that, at the same lateral displacement, the bending moment at beam end of the exterior joint is larger than that of the interior joint. When the lateral displacement reached 20 mm, bending-shear-induced diagonal cracks became obvious in the beams of the joints. The cracks propagated gradually and formed wider cracks. During the loading process, loud noise was heard due to the slippage of the steel reinforcements. When reaching the peak loads, the average lateral displacements (i.e., average of the push and pull displacements in a loading cycle) were 60.0 mm, 86.7 mm, and 89.4 mm for specimen SI-F, SE-F, and SE-C, respectively. With a further increase in the lateral displacement, concrete crushing and fall off was observed in beam ends, and the longitudinal rebars were exposed. In addition, a few minor cracks appeared in the joint core zone. At the peak load, the displacement of precast joint SE-F was almost the same as that of cast-in-place joint SE-C (within a 3% difference), indicating that the precast joint with five-spiral stirrups had comparable deformability to the cast-in-place counterpart.

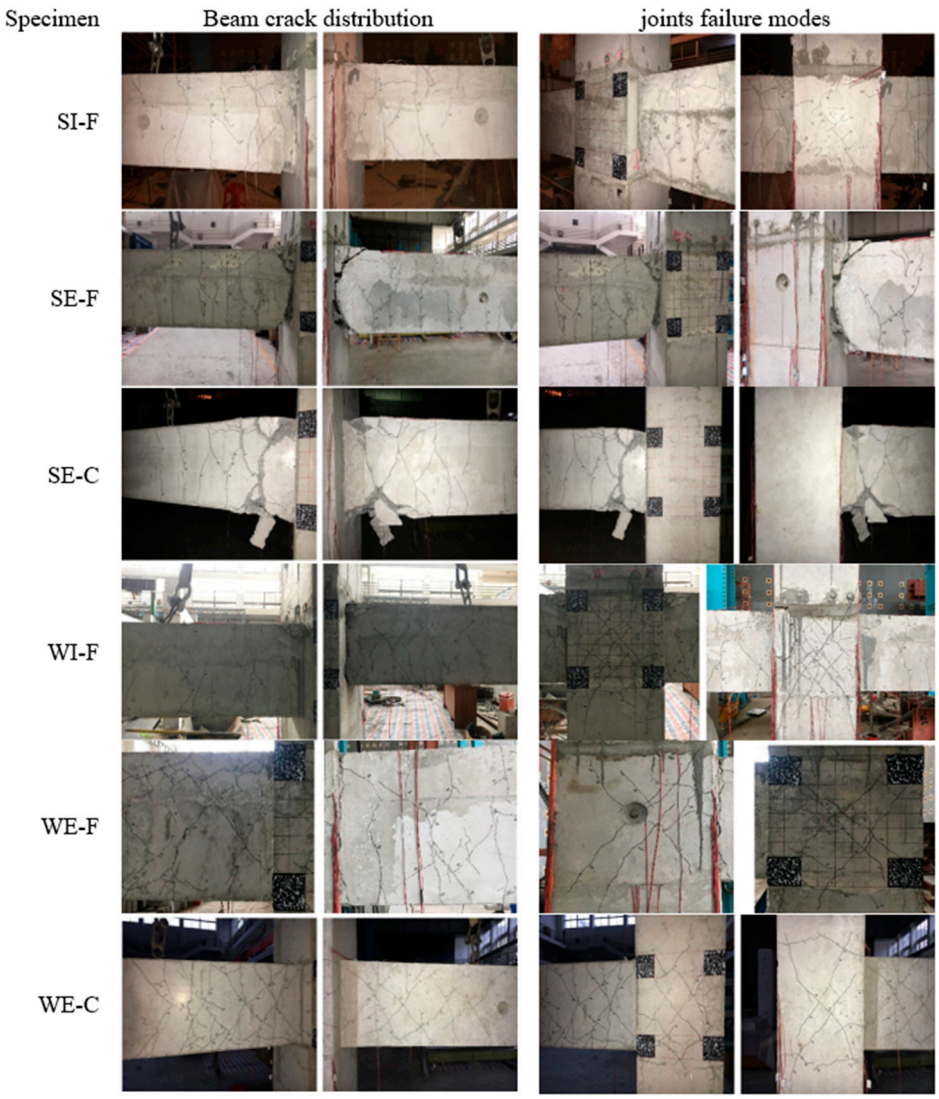

Figure 8. Cracking patterns and failure modes.

For specimens designed by the principle of weak joint and strong beam (i.e., WI-F, WE-F, and WE-C), failure in the joint core zone was observed. At the lateral displacement of 5 mm, cracks first appeared at the bottom of beam end of all the three joints. Owing to the increased reinforcement ratio in beams, the failure process of the specimens with joint failure was different from that of specimens with beam-end failure. When the lateral displacement reached 20 mm, vertical cracks were observed in the beam ends of precast specimens (WI-F and WE-F), and diagonal cracks appeared in the joint core region. Diagonal cracks started to appear in the core zone of the cast-in-place specimen (WE-C) when the lateral displacement reached 30 mm, showing a better integrity than the precast joints. There were two major diagonal cracks formed in the core region of specimen WI-F at the lateral displacement of 60 mm, and the maximum load was reached. The lateral displacements corresponding to the peak loads were 75.1 mm and 82.1 mm for specimen WE-F and WE-C, respectively. With a further increase in the lateral displacement, severe damage was then observed in the core regions of the specimens. In general, the damage was mainly located in the joint core region. Similarly, as the joints failed at beam ends, the exterior joints could reach a larger displacement than the interior joints.

3.2. Hysteresis Curves

Hysteresis curves (lateral load–lateral displacement curves) of the tested specimens are plotted in Figure 9. Generally, the shapes of the curves in the push and pull sides were similar. Owing to the existence of beams in both sides, the hysteresis curves of interior joints showed slightly better symmetry than those of exterior joints. In the initial stage, the loading and unloading curves were coincident, indicating that the joints were in the elastic state, and no residual deformation existed.

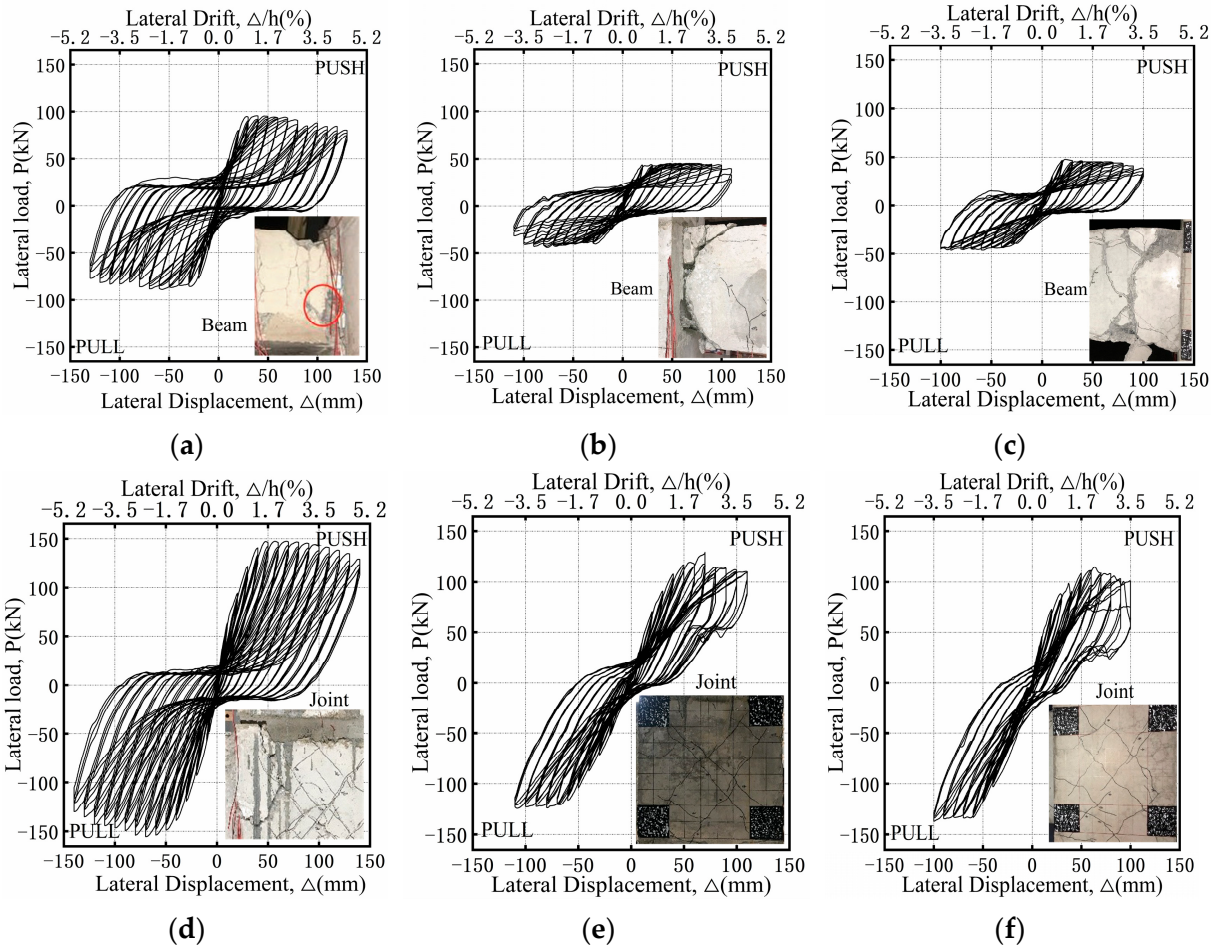

Figure 9. Load-mid span deflection relationships: (**a**) SI-F; (**b**) SE-F; (**c**) SE-C; (**d**) WI-F; (**e**) WE-F; (**f**) WE-C.

As shown in Figure 9, the pinching effect is more significant for specimens that failed at the joint core zone, proving that the joints that failed at beam ends had more energy dissipation and higher ductility. In the initial loading process, deformation mainly occurred in the beams. Nevertheless, with the increase in the applied load, damage was concentrated in the joint core region for specimens with joint failure mode (i.e., WI-F, WE-F, and WE-C), owing to the low shear resistance of the core region. The comparison of the hysteresis curves demonstrated the reasonability of design codes that adopted the concept of strong joint and weak beam for connection design to ensure the capability of dissipating energy and high ductility. For specimens that failed at the joint core region, the hysteresis curves of precast and cast-in-place specimens (i.e., WE-F and WE-C) were very similar. Nevertheless, the hysteresis curve of specimen SE-F is fuller than that of its cast-in-place counterpart (i.e., SE-C), indicating the beneficial effect of the five-spiral stirrups by offering a higher confinement on the concrete.

3.3. Skeleton Curves

The skeleton curve refers to the envelope of the hysteresis curve, which provides a simplified representation of the overall behavior of the hysteresis curve without considering the detailed loading and unloading path. Skeleton curves of the tested specimens are summarized in Figure 10. During the initial loading stage, the skeleton curve was in linear shape as the specimen was in elastic. In general, the skeleton curves of the precast and cast-in-place specimens were very similar, indicating that the precast joint with five-spiral stirrups had comparable load-bearing capacity of its cast-in-place counterpart. In addition, the skeleton curves were symmetric with respect to the origin, showing the same seismic performance in both directions. Owing to the contribution of the beams, the interior joints that had two beams had higher stiffness and load-bearing capacity than the exterior joints with only one beam.

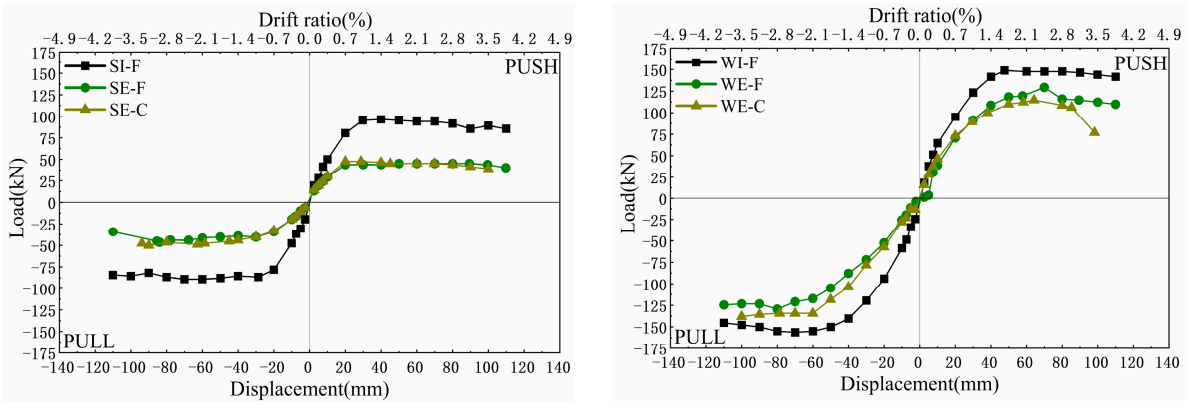

Figure 10. Skeleton curves of specimens: (**a**) beam-end failure group; (**b**) joint failure group.

As shown in Figure 10, specimens that failed in the joint core region (i.e., WI-F, WE-F, and WE-C) have higher ultimate capacities than specimens that failed at beam ends. This is due to the higher reinforcement ratio of beams for those specimens. At peak load, the displacement of joint failure group was larger than that of the bend end failure group. During the post-peak stage, the load drop was slow for the specimens. Nevertheless, there was a sudden load drop by 29.1% in specimen WE-C at the lateral displacement of 80–100 mm. The load of the corresponding precast specimen WE-F was only about 3.1%. Therefore, the five-spiral stirrup could obviously avoid the sudden load drop of specimens that failed in the joint core zone, and this is mainly caused by the high confinement induced by the spiral stirrups.

3.4. Ductility

The ductility coefficient is a parameter used to quantify the ductility of a material or structure. The ductility coefficient (μ) is calculated as [29,30]:

$$\mu = \frac{\Delta_u}{\Delta_y} \tag{1}$$

where Δ_u is the ultimate displacement, corresponding to 85% of the peak load P_m in the post-peak stage, and Δ_y is yield displacement. In this study, the yield displacement was determined by using the energy equivalence method, as shown in Figure 11. The equivalent elastic–perfect plastic bilinear curve was determined by setting the intersection area S1 as equal to S2. The intersect, Y, was then regarded as the yield point (Δ_y, P_y). Feature points in the skeleton curves and the ductility coefficient (μ) of the tested specimens are summarized in Table 5, where P_y is the yield capacity, P_m is the peak capacity, P_u is the capacity at Δ_u, Δ_y is the yield displacement, Δ_m is the displacement corresponding to P_m, and Δ_u is the

ultimate displacement. It is necessary to mention that the values in Table 5 are the average of the values from the push and pull sides of the skeleton curves.

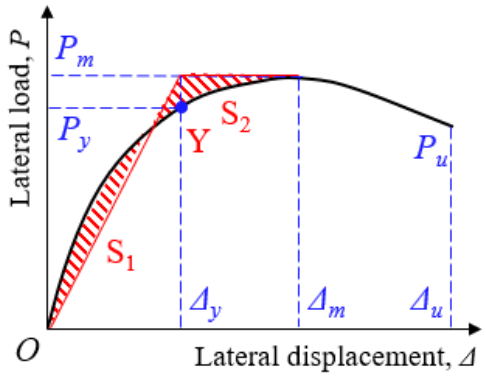

Figure 11. Schematic diagram of the energy equivalence method.

Table 5. Feature points and ductility coefficients.

No.	P_y (kN)	Δ_y (mm)	P_m (kN)	Δ_m (mm)	P_u (kN)	Δ_u (mm)	μ
SI-F	82.1	22.5	91.6	60.0	77.8	129.3	5.8
SE-F	40.0	24.6	45.8	86.7	38.9	104.1	4.2
SE-C	41.3	25.4	48.8	59.4	41.5	97.2	3.8
WI-F	132.9	35.0	152.6	58.8	129.7	138.5	4.0
WE-F	116.3	53.4	129.4	75.1	110.0	110.0	2.1
WE-C	110.7	44.9	126.3	82.2	107.4	94.6	2.1

As shown in Table 5, the ductility index of specimens that failed in beam ends are higher than those of specimens that failed in the joint core region, exhibiting higher ductility and deformability. In addition, the interior joints had a higher ductility index than the exterior joints.

The small difference of the peak loads (P_m) between the precast and cast-in-place joints (less than 3.1%) indicated that the effect of the construction method on the load-bearing capacity is negligible. Nevertheless, the lateral displacements at peak load (Δ_m) were greatly different for precast and cast-in-place specimens. The design principle (i.e., intended failure modes) could also affect the Δ_m. The Δ_m of specimen SE-F is 33.3% larger than that of SE-C (beam-end failure), whereas Δ_m of WE-F is 8.6% less than that of WE-C (joint failure). It was found that the ductility index of precast specimens was not less than that of cast-in-place specimens: SE-F was 10.5% larger than SE-C, and WE-F was comparable to WE-C in terms of the μ. In conclusion, precast joints with five-spiral stirrups had comparable ductility and plastic deformation performance, under cyclic loading, to their cast-in-place counterparts.

3.5. Energy Dissipation

The equivalent viscous damping coefficient, h_e, was adopted to quantify the energy dissipation capacity of the structure during an earthquake. It is defined as the ratio of energy input to the energy dissipated by the specimen:

$$h_e = \frac{1}{2\pi} \times \frac{S(ABCD)}{S(\Delta OBE + \Delta ODF)} \quad (2)$$

where $S(ABCD)$ is the area enveloped by the hysteresis loop, and $S(OBE)$ and $S(ODF)$ represent the area of the triangles OBE and ODF in Figure 12, respectively.

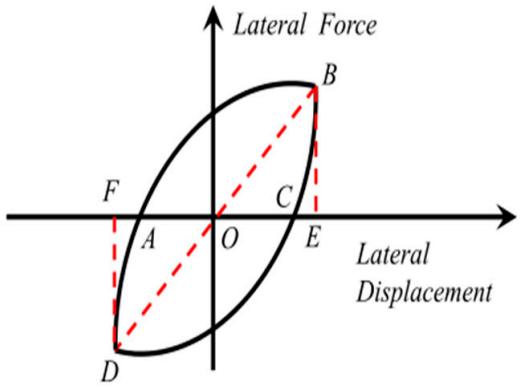

Figure 12. Schematic diagram of equivalent viscous damping coefficient.

The h_e of the specimens in each hysteresis loop is summarized in Figure 13, where the horizontal axis is the maximum lateral displacement (average of the push and pull side) within each loop. In the initial loading stage, as the specimens were in elastic state, h_e is very small (h_e = 0.05~0.1), indicating the low energy dissipation capacity. For specimens that failed at beam ends, h_e increased obviously from the lateral displacement of 20 mm, whereas this occurred at 40 mm displacement for specimens that failed in the joint region. As shown in Figure 13, the ranges of h_e are 0.05~0.26 and 0.05~0.12 for the beam-end failure group and joint failure group, respectively. Specimens that failed at beam ends exhibited a higher energy dissipation capacity than the specimens with joint core region failure. For the beam-end failure group, h_e of the precast specimen (SE-F) was larger than that of the cast-in-place specimen (SE-C), indicating that the five-spiral stirrups could enhance the ductility and plasticity by offering high confinement on concrete. Nevertheless, for specimens that failed at joint core region, h_e of the precast and cast-in-place specimens was similar. This indicates that, for the joint failure group specimens, the five-spiral stirrups have no significant improvement effect on the energy dissipation capacity of prefabricated beam–column joints.

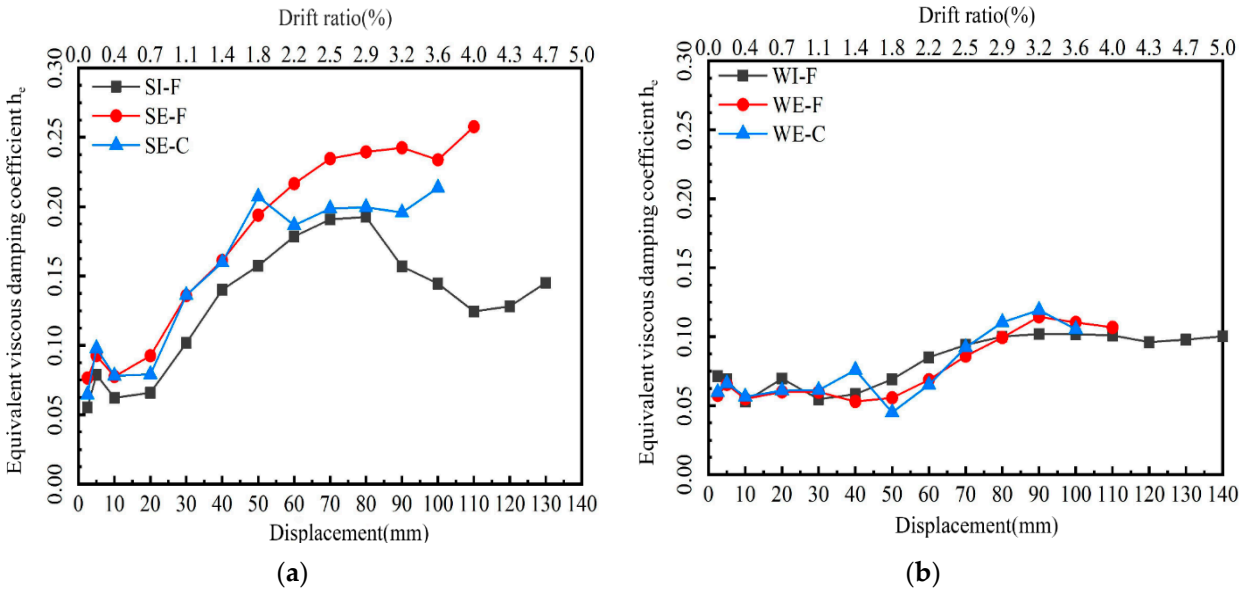

Figure 13. Equivalent viscous damping coefficient of joins: (**a**) beam-end failure group; (**b**) joint failure group.

3.6. Strength Degradation

Strength of the beam–column joint deteriorates, owing to the cyclic loading. In this study, strength degradation was represented by the strength degradation coefficient, which is calculated as:

$$\alpha_i^j = \frac{P_i^j}{P_1^j} \tag{3}$$

where α_i^j is the degradation coefficient in the ith cycle of jth loading step (i = 2, 3 and j = 1, 2, 3, . . .), P_i^j is the maximum applied load in the ith cycle of jth step, and P_1^j is the maximum load in the first loop of jth step. A larger value of α_i^j represents less degradation of the strength induced by the cyclic loading. The α_i^j of the tested specimens is summarized in Figure 14.

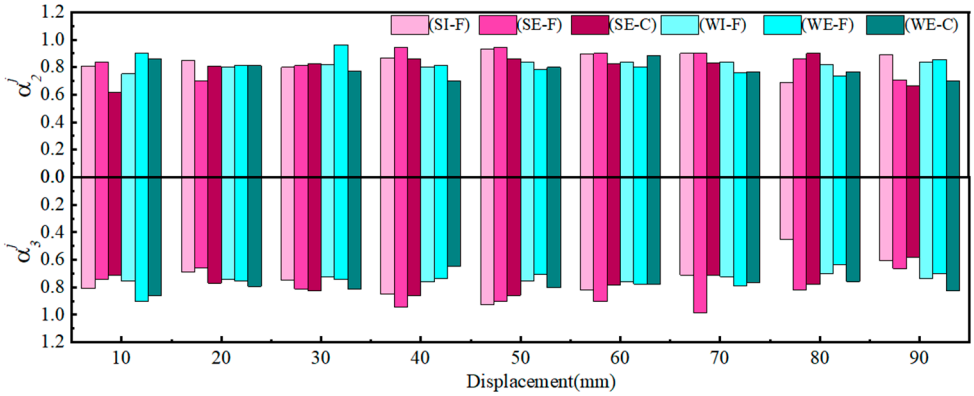

Figure 14. Strength degeneration coefficient.

With the increase in displacement, the strength degradation coefficients of all specimens exhibited an overall trend of initially increasing and then decreasing, but they all remained above 0.5, indicating good load-bearing capacity of the specimens. In the displacement range of 60–90 mm, there was a significant decrease in α_i^j, which is attributed to the severe damage to the joint regions. In the beam-end failure group, during the initial loading stage, the strength degradation coefficient of the precast joint SE-F is higher than that of the cast-in-place joint SE-C. This indicated that the prefabricated joint exhibited less strength degradation during the initial loading stage compared to the cast-in-place joint. After the displacement exceeded 40 mm, the values of α_i^j for the beam-end failure group specimens began to increase, indicating a reduction in the degree of strength degradation. For most displacements, the values of α_i^j of the precast specimens were higher than those of the cast-in-place specimens. Taking a displacement of 50 mm as an example, the average values of α_i^j for the prefabricated joint SE-F were 7.0% higher than those of the cast-in-place joint SE-C. This suggested that, when designing the beam–column joints for beam-end failure, the configuration of five-spiral stirrups in the core region of the joint could mitigate the degree of strength degradation in prefabricated beam–column joints, surpassing the performance of cast-in-place joints. For the joint failure group specimens, at displacements of 10 mm, 20 mm, and 30 mm, the average values of α_i^j for the prefabricated joint WE-F were 2.1%, −1.3%, and 12.5% higher than those of the cast-in-place joint WE-C, respectively. This indicated that the configuration of five-spiral stirrups had a certain mitigating effect on the strength degradation of the beam–column joints when designed for the joint failure mode.

3.7. Stiffness Degradation

The secant stiffness (K_i) can represent the change of stiffness of a structure under seismic loading. This study used K_1 (the stiffness of the specimen during the first cycle) as the stiffness of the specimen at this displacement level, and it plotted a stiffness–degradation

curve, as shown in Figure 15. The stiffness–degradation curve reflects the cumulative damage level of the structure during seismic loading.

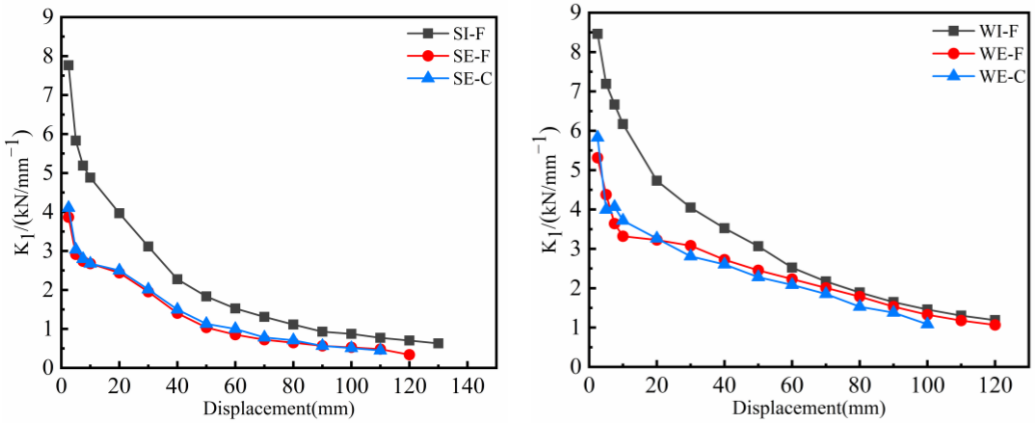

(**a**) (**b**)

Figure 15. Stiffness–degeneration curves: (**a**) beam-end failure group; (**b**) joint failure group.

In the initial loading stage, significant stiffness degradation was observed in all specimens. This is because the concrete and reinforcements had not yet achieved good synergy. In the later stages of loading, the stiffness degradation of both groups of specimens tended to decrease slowly. Throughout the loading process, the stiffness values of the interior joints were higher than those of the exterior joints. Additionally, the initial stiffness of the beam-end failure group specimens ranged from 3.9–7.8 kN/mm, while the initial stiffness of the joint failure group specimens ranged from 5.4–8.5 kN/mm. The higher stiffness of specimens that failed in the joint region was mainly contributed by the higher reinforcement ratio in the beams.

For the beam-end failure group specimens, the stiffness–degradation curve of the prefabricated joint SE-F was similar to that of the cast-in-place joint SE-C throughout the entire loading process. This indicated that, as the displacement increased, the cracking level and yield state of the reinforcements were similar during the loading process of the joints designed as "strong joint weak beam" (i.e., failed at beam ends). For the joint failure group, after a displacement of 20 mm, the K_1 values of the prefabricated joint WE-F were consistently higher than those of the cast-in-place joint WE-C. This indicated that the configuration of five-spiral stirrups in the core region of the joint could improve the stiffness to some extent.

3.8. Deformation of the Joint Core Zone

When the core region of a joint undergoes shear deformation, it transforms from a rectangular shape into a diamond shape [31]. The deformation coefficient γ of the core region is calculated using Equation (4), and a schematic diagram of the calculation is shown in Figure 16, where Δ_1–Δ_4 represent the displacements at the four corners of the core region, which are obtained through displacement measurements. a and b represent the lengths of the two sides of the core region. The values of γ for all beam–column joints are shown in Figure 17. It is necessary to mention that, due to human error in arranging LVDT during the experiment, the deformation data Δ of the joint core zone of the beam–column joint SI-F was too large, and γ was significantly larger than other joint specimens. Therefore, the deformation of the joint core zone of the joint was not discussed.

$$\gamma = \frac{1}{2}(\Delta_1 + \Delta_2 + \Delta_3 + \Delta_4)\frac{\sqrt{a^2 + b^2}}{ab} \quad (4)$$

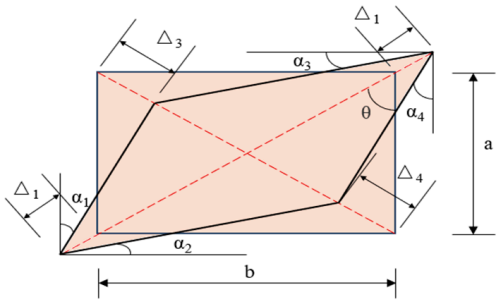

Figure 16. Shear deformation calculation of the joint core zone.

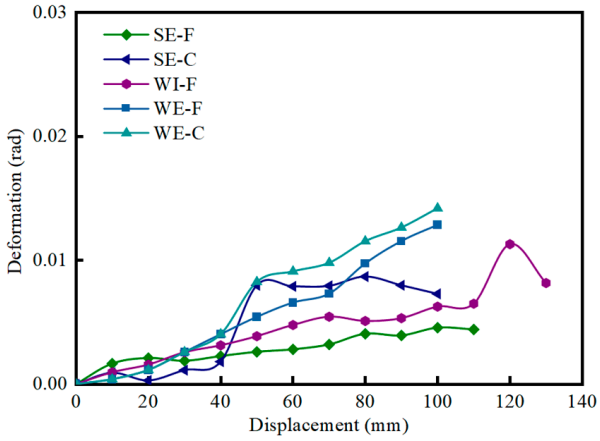

Figure 17. Shear deformation of the joint core.

In the initial loading stage, the deformation of the core region in all specimens was relatively small, resulting in small values of γ. As the loading progressed, the shear deformation of the joint core region increased gradually. In the initial stage, the beam-end failure group and the joint failure group exhibited similar levels of shear deformation in their core regions. However, as the displacement increased, the values of γ for the beam–column joints WE-F and WE-C became larger than those of the joints SE-F and SE-C, and the difference increased with the increase in displacement. Taking a displacement of 100 mm as an example, the values of γ for the joints WE-F and WE-C were 182.0% and 94.9% higher, respectively, than those of the joints SE-F and SE-C. This indicated that the beam–column joints designed for joint failure mode exhibited greater shear deformation in their core regions, which explained the occurrence of shear failure in those regions. Furthermore, at a displacement of 100 mm, the values of γ for the cast-in-place specimens SE-C and WE-C were 59.9% and 10.5% higher, respectively, than those of the precast specimens SE-F and WE-F. This indicated that the core region of the precast joints, reinforced with five-spiral stirrups, exhibited stronger resistance to shear deformation compared to the corresponding cast-in-place joints.

4. Capacity Prediction

For a beam–column joint, shear force in the core region could be derived from the bending moment, as shown in Equation (5):

$$V_{j,exp} = \sum \frac{M_b}{h_{b0} - a'_s}\left(1 - \frac{h_{b0} - a'_s}{H_c - h_b}\right) \quad (5)$$

where $V_{j,exp}$ is the shear force in the joint, ΣM_b is the summation of the bending moments in beams, H_c is the distance between the inflection points of the upper and lower columns, h_b and h_{b0} are height and effective height of the beam, respectively, and a'_s is the distance between the extreme compressive fiber and the centroid of the compressive reinforcements.

Based on design code [32], the beam-end bending moment capacity of the joints designed for beam-end failure could be calculated as:

$$M_{u,cal} = \alpha_1 f_c b x \left(h_0 - \frac{x}{2}\right) \tag{6}$$

where $M_{u,cal}$ is the predicted moment capacity, f_c is the concrete compressive strength, h_0 is the effective depth of the beam section, x is the height of the compressive zone of the concrete beam section, and α_1 is the graphic coefficient of the equivalent rectangular stress diagram, taken as 1.0 when the concrete strength grade does not exceed C50.

For cast-in-place joints, the shear capacity could be calculated as:

$$V_j = 1.1\eta_j f_t b_j h_j + 0.05\eta_j N \frac{b_j}{b_c} + f_{yv} A_{svj} \frac{h_{b0} - a_s{}'}{s} \tag{7}$$

Based on design code [33], shear capacity of precast joints with five-spiral stirrups shall be calculated as:

$$V_j = 1.1\eta_j f_t b_j h_j + 0.05\eta_j N \frac{b_j}{b_c} + \frac{\pi}{2} \frac{f_{yv} A_{svj}}{s} D_1 \tag{8}$$

where η_j is the coefficient considering the effect of beams on the joints' shear capacity, taken as 1.0 for the interior joint and 0.67 for the exterior joint, f_t is the calculated value of the axial tensile strength of concrete, f_{yv} is the calculated tensile strength value of the stirrup, A_{svj} is the cross-section area of stirrups within the effective width of beams, s is the spacing of stirrups, N is the axial force on columns, b_j and h_j are the width and height of the cross-section, b_c is the height of column section, and D_1 is the diameter of the large spiral stirrup.

The predicted moment capacity and shear capacity of the tested joints are listed in Tables 6 and 7, respectively, and the accuracy is assessed by comparison to experimental capacities that were the average from the push and pull sides in the hysteresis curves. During the calculation, concrete strength and steel rebar strength were from the material test, b_c = 450 mm, h_j = 250 mm, $N = 0.1 f_c b_c h_c$, H_c = 3.2 m, a_s = 35 mm, and D_1 = 380 mm. As shown in Table 6, the predicted bending moment of the joints that failed at beam ends is less than the experimental capacity by 16.1%~30.3%. For joints that failed in the joint core region, the predicted shear capacity is less than the experimental capacity by 9.70%−16.8%. Comparison of the experimental and predicted capacities suggests that the seismic performance of the precast joint with five-spiral stirrups could act as the requirement from the design code with enough of a safety margin.

Table 6. Comparison of the experimental and predicted moment capacities.

Specimen	Peak Load P (kN)	Experimental Moment Capacity $M_{u,exp}$ (kN·m)	Predicted Moment Capacity $M_{u,cal}$ (kN·m)	$M_{u,exp}/M_{u,cal}$
SI-F	91.6	120.70	103.99	1.161
SE-F	45.8	126.27	103.99	1.214
SE-C	48.8	134.54	103.99	1.294

Table 7. Comparison of the experimental and predicted shear capacities.

Specimen	Peak Load P (kN)	Experimental Shear Capacity $V_{j,exp}$ (kN)	Predicted Shear Capacity $V_{j,cal}$ (kN)	$V_{j,exp}/V_{j,cal}$
WI-F	152.6	1060.37	918.01	1.155
WE-F	129.4	887.74	809.10	1.097
WE-C	126.3	866.48	741.55	1.168

5. Conclusions

This paper proposed a novel precast beam–column joint with five-spiral stirrups. There were six full-scale beam-column joint specimens tested for their seismic performance, considering design criteria, joint types, construction methods, and types of stirrups in the joint core region as parameters. This paper extensively analyzed the failure modes, hysteresis curves, skeleton curves, ductility coefficients, energy dissipation capacity, strength degradation, stiffness degradation, and deformation capacity of the joint core region for each specimen, and it predicted the load-bearing capacity of the joints. The following conclusions are drawn:

(1) By using the five-spiral stirrups, precast concrete beam–column joint has comparable deformation capacity to its cast-in-place counterpart. Failure modes of the precast and cast-in-place joints were similar, and the difference of the displacements at peak loads of them was less than 3.0%.

(2) Joints with beam-end failure exhibited more energy dissipation and higher ductility than the joints that failed in the core region. Owing to the high reinforcement ratio in beams, the joint failure group specimens had higher stiffness and load-bearing capacity. The interior joint with two beams had higher ductility than the exterior joint with one beam.

(3) Due to the good restraining effect of the five-spiral stirrups, concrete crushing is delayed. For joints designed as beam-end failures, seismic performance (e.g., energy dissipation capacity, plastic deformation capacity, ductility, strength degradation, stiffness degradation, shear deformation resistance level) of precast joints with five-spiral stirrups was better than that of the corresponding cast-in-place joints. Among them, the ductility, strength degradation and shear deformation resistance level of the joints increased by 10.5%, 7.0%, and 59.9%, respectively. For joints designed as joint region failures, the precast joints had comparable seismic behavior to cast-in-place joints. In addition, the five-spiral stirrups could effectively avoid the sudden load drop of the precast joints under cyclic loading. In summary, the seismic performance of the proposed precast joint is as good as the cast-in-place joints, and the precast joint could reduce the carbon emission. It has significant value for application and promotion in civil engineering.

(4) Based on the current design code, the experimental moment capacity and shear capacity of the joints were, on average, 22.6% and 14.0% higher than the predicted capacities, respectively. Therefore, the design code could be used for the design of the proposed joint type with an adequate safety margin.

Author Contributions: Conceptualization, J.Z., Z.P. and H.Z.; Data curation, X.D., C.Z. and Z.X.; Formal analysis, J.Z. and L.X.; Funding acquisition, L.L.; Investigation, J.Z. and L.L.; Methodology, J.Z. and Z.X.; Project administration, L.L. and F.L.; Resources, L.L. and F.L.; Software, Z.Q.; Supervision, Z.X., L.L. and F.L.; Writing—original draft, J.Z. and Z.P.; Writing—review & editing, J.Z. and Z.P. All authors have read and agreed to the published version of the manuscript.

Funding: This research was funded by the National Natural Science Foundation of China under Grant No. 12032009.

Data Availability Statement: The original data will be available upon requirement.

Acknowledgments: The authors gratefully thanks all technical personnel from the Structural Laboratory of Guangdong University of Technology for their assistance during the experiment.

Conflicts of Interest: The authors declare no conflict of interest.

References

1. Li, D.Z.; Huang, G.Y.; Zhu, S.Y.; Chen, L.; Wang, J.B. How to peak carbon emissions of provincial construction industry? Scenario analysis of Jiangsu Province. *Renew. Sust. Energ. Rev.* **2021**, *144*, 110953. [CrossRef]
2. Hou, H.M.; Feng, X.Y.; Zhang, Y.; Bai, H.T.; Ji, Y.J.; Xu, H. Energy-related carbon emissions mitigation potential for the construction sector in China. *Environ. Impact. Asses.* **2021**, *89*, 106599. [CrossRef]

3. Yang, Z.; Chen, H.; Mi, L.; Li, P.P.; Qi, K. Green building technologies adoption process in China: How environmental policies are reshaping the decision-making among alliance-based construction enterprises? *Sustain. Cities Soc.* **2021**, *73*, 103122. [CrossRef]
4. Zhao, Y.; Liu, L.; Yu, M. Comparison and analysis of carbon emissions of traditional, prefabricated, and green material buildings in materialization stage. *J. Clean. Prod.* **2023**, *406*, 137152. [CrossRef]
5. Wang, H.S.; Marino, E.M.; Pan, P.; Liu, H.; Nie, X. Experimental study of a novel precast prestressed reinforced concrete beam-to-column joint. *Eng. Struct.* **2018**, *156*, 68–81. [CrossRef]
6. Jin, R.Y.; Hong, J.K.; Zuo, J. Environmental performance of off-site constructed facilities: A critical review. *Energy Build.* **2020**, *207*, 109567. [CrossRef]
7. Dong, Y.H.; Jaillon, L.; Chu, P.; Poon, C.S. Comparing carbon emissions of precast and cast-in-situ construction methods—A case study of high-rise private building. *Constr. Build. Mater.* **2015**, *99*, 39–53. [CrossRef]
8. Sandanayake, M.; Luo, W.K.; Zhang, G.M. Direct and indirect impact assessment in off site construction—A case study in China. *Sustain. Cities Soc.* **2019**, *48*, 101520. [CrossRef]
9. Rong, X.; Yang, H.W.; Zhang, J.X. Experimental study of precast beam-to-column joints with steel connectors under cyclic loading. *Adv. Struct. Eng.* **2020**, *23*, 2822–2834. [CrossRef]
10. Xu, L.H.; Zhang, G.; Xiao, S.J.; Li, Z.X. Development and experimental verification of damage controllable energy dissipation beam to column connection. *Eng. Struct.* **2019**, *199*, 109660. [CrossRef]
11. Senel, S.M.; Palanci, M.; Kalkan, A.; Yılmaz, Y. Investigation of shear and overturning safety of hinged connections in existing precast buildings. *Tek. Dergi.* **2013**, *24*, 6505–6528.
12. Ozden, S.; Akpinar, E.; Erdogan, H.; Atalay, H.M. Performance of precast concrete structures in October 2011 Van earthquake, Turkey. *Mag. Concrete Res.* **2014**, *66*, 543–552. [CrossRef]
13. Deng, M.K.; Ma, F.D.; Song, S.F.; Lü, H.; Sun, H.Z. Seismic performance of interior precast concrete beam-column connections with highly ductile fiber-reinforced concrete in the critical cast-in-place regions. *Eng. Struct.* **2020**, *210*, 110360. [CrossRef]
14. Guan, M.S.; Xiao, J.G.; Wang, Y.; Zhang, Y.; Liang, Z.Q.; Lai, Z.C. Seismic behavior of innovative precast hybrid steel reinforced concrete beam-column connections. *J. Constr. Steel. Res.* **2023**, *203*, 107817. [CrossRef]
15. Huang, W.; Hu, G.X.; Zhang, J.R. Experimental study on the seismic performance of new precast concrete beam-column joints with replaceable connection. *Structures* **2022**, *35*, 856–872. [CrossRef]
16. Xu, C.X.; Peng, S.; Liu, X.Q.; Wang, C.F.; Xu, Q.Q. Analysis of the seismic behavior of CFRP-strengthened seismic-damaged composite steel-concrete frame joints. *J. Build. Eng.* **2020**, *28*, 101057. [CrossRef]
17. Villar-Salinas, S.; Guzmán, A.; Carrillo, J. Performance evaluation of structures with reinforced concrete columns retrofitted with steel jacketing. *J. Build. Eng.* **2021**, *33*, 101510. [CrossRef]
18. Zhang, Z.Y.; Ding, R.; Nie, X.; Fan, J.S. Seismic performance of a novel interior precast concrete beam-column joint using ultra-high performance concrete. *Eng. Struct.* **2020**, *222*, 111145. [CrossRef]
19. Xiong, Z.; Zheng, J.H.; Chen, Z.P.; Huang, Y.B.; Wang, Z.M.; Chen, J.Y.; Lin, L.H.; Li, L.J.; Qiao, S.H.; Liu, F. Seismic behavior and design method of seawater sea-sand concrete reinforced with GFRP and five interlocking spirals. *Eng. Struct.* **2023**, *291*, 116410. [CrossRef]
20. Fang, S.; Li, L.J.; Luo, Z.P.; Fang, Z.C.; Huang, D.C.; Liu, F.; Wang, H.L.; Xiong, Z. Novel FRP interlocking multi-spiral reinforced-seawater sea-sand concrete square columns with longitudinal hybrid FRP–steel bars: Monotonic and cyclic axial compressive behaviours. *Compos. Struct.* **2023**, *305*, 116487. [CrossRef]
21. Ou, Y.C.; Li, J.Y.; Roh, H. Shear strength of reinforced concrete columns with five-spiral reinforcement. *Eng. Struct.* **2021**, *233*, 111929. [CrossRef]
22. Yin, Y.L.; Wang, J.C.; Wang, P.H. Development of multi-spiral confinements in rectangular columns for construction automation. *J. Chin. Inst. Eng.* **2012**, *35*, 309–320. [CrossRef]
23. Fang, S.; Li, L.J.; Lin, L.H.; Wang, H.L.; Fang, Z.C.; Li, Z.W.; Xiong, Z.; Liu, F. FRP interlocking multi-spiral reinforced square concrete columns: A promising compression application for marine engineering. *Eng. Struct.* **2021**, *244*, 112733. [CrossRef]
24. Wu, T.L.; Ou, Y.C.; Yin, Y.L.; Wang, J.C.; Wang, P.H.; Ngo, S.H. Behavior of oblong and rectangular bridge columns with conventional tie and multi-spiral transverse reinforcement under combined axial and flexural loading. *J. Chin. Inst. Eng.* **2013**, *36*, 980–993. [CrossRef]
25. Yin, Y.L.; Wang, R.Z.; Wu, Z.L.; Tang, X.M. The survey of experiments in automated forming multi-spiral stirrup columns. *City House* **2015**, 114–118. (In Chinese)
26. *GB/T 50081-2002*; Standard for Test Method of Mechanical Properties on Ordinary Concrete. China Architecture & Building Press: Beijing, China, 2003.
27. *GB/T 228-2010*; Metallic Materials-Tensile Testing at Ambient Temperature. China Architecture & Building Press: Beijing, China, 2010.
28. *ACI 374.1-05*; Acceptance Criteria for Moment Frames Based on Structural Testing and Commentary. ACI Committee 374: Farmington Hills, MI, USA, 2019.
29. Tang, J.R. *Seismic Resistance of Joints in Reinforced Concrete Frames*; Southeast University Press: Nanjing, China, 1989.
30. Shen, J.M.; Zhou, X.Y. *Seismic Eengineering*; China Building Industry Press: Beijing, China, 2000.
31. Qin, Y.; Chen, Z.H.; Han, N. Research on design of through-diaphragm connections between CFRT columns and HSS beams. *J. Constr. Steel. Res.* **2014**, *114*, 146–156. [CrossRef]

32. *GB 50010-2010*; Code for Design of Concrete Structures. China Architecture & Building Press: Beijing, China, 2010.
33. *T/CECS 512-2018*; Technical Specification for Application of Multi Spiral Stirrup Column. China Planning Press: Beijing, China, 2018.

Disclaimer/Publisher's Note: The statements, opinions and data contained in all publications are solely those of the individual author(s) and contributor(s) and not of MDPI and/or the editor(s). MDPI and/or the editor(s) disclaim responsibility for any injury to people or property resulting from any ideas, methods, instructions or products referred to in the content.